Physics of Fluids

Vortex system around a step cylinder in a turbulent flow field

Cite as: Phys. Fluids **33**, 045112 (2021); https://doi.org/10.1063/5.0041234
Submitted: 21 December 2020 . Accepted: 22 February 2021 . Published Online: 07 April 2021

Cai Tian (田偲), Fengjian Jiang (蒋奉兼), Bjørnar Pettersen, and Helge I. Andersson

COLLECTIONS

This paper was selected as an Editor's Pick

Vortex system around a step cylinder in a turbulent flow field

Cite as: Phys. Fluids **33**, 045112 (2021); doi: 10.1063/5.0041234
Submitted: 21 December 2020 · Accepted: 22 February 2021 ·
Published Online: 7 April 2021

View Online Export Citation CrossMark

Cai Tian (田偲),[1] Fengjian Jiang (蒋奉兼),[2,a)] Bjørnar Pettersen,[1] and Helge I. Andersson[3]

AFFILIATIONS

[1]Department of Marine Technology, Norwegian University of Science and Technology (NTNU), NO-7491 Trondheim, Norway
[2]SINTEF Ocean, NO-7052 Trondheim, Norway
[3]Department of Energy and Process Engineering, NTNU, NO-7491 Trondheim, Norway

[a)]Author to whom correspondence should be addressed: fengjian.jiang@sintef.no

ABSTRACT

The vortex system around the step surface of a step cylinder with a diameter ratio $D/d = 2$ at Reynolds number (Re_D) 3900 was investigated by directly solving the three-dimensional Navier–Stokes equations. Formation mechanisms and vortex dynamics of the complex vortex system were studied by performing a detailed investigation of both the time-averaged and instantaneous flow fields. For the time-averaged flow, including the known *junction* and *edge vortices*, in total, four horseshoe vortices were observed to form above the step surface in front of the upper small cylinder. The crossflow width of the four horseshoe vortices varies differently as they convect downstream. Moreover, we captured a pair of *base vortices* and a backside horizontal vortex in the rear part of the step surface behind the small cylinder. For the instantaneous flow, hairpin vortices were found to form between the legs of two counter-rotating horseshoe vortices located on the same side of the step cylinder. Furthermore, in the small step cylinder wake, Kelvin–Helmholtz vortices were observed to shed at an unexpectedly high shedding frequency.

I. INTRODUCTION

The flow around a uniform circular cylinder has been a popular research topic for several decades because of its simple geometry and vast flow phenomena in its wakes. As the Reynolds number $Re_D = UD/\nu$ varies (D represents the diameter of the circular cylinder, U and ν are the free-stream velocity and the kinematic viscosity, respectively), the cylinder wake flow exhibits distinctly different behaviors.[1,2] When Re_D is less than 5, there is no flow separation around the cylinder. As Re_D increases to the range $5 < Re_D < 40$, the flow separates on the cylinder wall to form a fixed pair of vortices behind the cylinder, and there is no vortex shedding. For $40 < Re_D < 180$, periodic two-dimensional vortex shedding occurs. When Re_D exceeds 180, the wake becomes three-dimensional. Williamson[1] reported the well-known mode A and mode B at $Re_D = 184 - 194$ and $Re_D = 200 - 250$, respectively. When the Reynolds number becomes larger than $Re_D \approx 300$, the cylinder wake flow becomes completely turbulent. The boundary layer over the cylinder surface stays laminar in a wide Reynolds number regime $300 < Re_D < 2 \times 10^5$, which is known as the subcritical flow regime.[2] In this regime, the particular Reynolds number 3900 is a benchmark, at which there are many accurate numerical simulations[3–6] and experimental studies.[7,8]

Besides the circular cylinder, due to the extensive applications in marine engineering, e.g., the underwater hull of Single Point Anchor Reservoir (SPAR)-buoy floating offshore wind turbines[9] and the steel lazy wave risers,[10,11] the flow around the step cylinder illustrated in Fig. 1(a) has also attracted attention in recent years. In 1992, Lewis and Gharib[13] experimentally investigated the wake of a single-step cylinder with $1 < D/d < 2$ at Reynolds number $Re_D = UD/\nu$ in the range $35 < Re_D < 200$. They identified three vortex interaction modes, namely *direct mode* when $D/d < 1.25$, *indirect mode* when $D/d > 1.55$, and *transition mode* when $1.25 < D/d < 1.55$. In *direct mode*, vortices shed from the small cylinder directly interact with those from the large cylinder in a narrow region. The wake is dominated by two frequencies f_S and f_L corresponding to shedding frequencies of the spanwise vortex structures behind the small and large cylinder, respectively. In the *indirect mode*, one more frequency f_3 (which is also referred to as f_N by Dunn and Tavoularis[14]) was identified in a so-called modulation zone, in which no direct interaction was found between vortices with f_S and f_L. Dunn and Tavoularis[14] validated the *indirect mode* through experimental investigations in the wake of a step cylinder with $D/d \approx 2$ at $63 < Re_D < 1100$. Based on the three dominating frequency components behind the step cylinder, they identified three types of spanwise vortex cells: (1) S-cell vortex with the

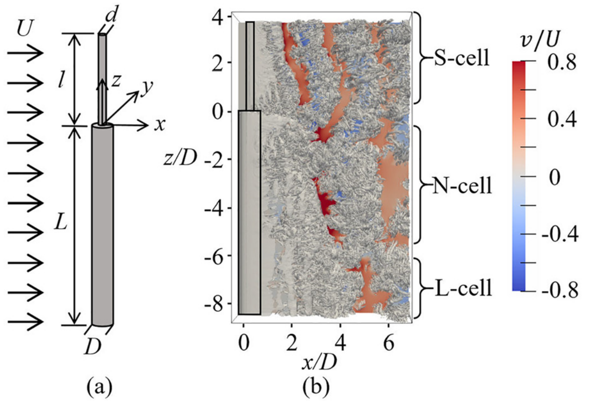

FIG. 1. (a) A sketch of the step cylinder geometry. The diameters of the small and large cylinders are d and D, respectively. l and L denote the length of the small and large cylinders. The origin is located at the center of the interface between the small and large cylinders. The uniform incoming flow U is in the positive x-direction. The three directions are referred to as streamwise (x-direction), crossflow (y-direction), and spanwise (z-direction). (b) Perspective view of the instantaneous wake behind a single-step cylinder with $D/d = 2$ at $Re_D = 3900$, taken at an arbitrary moment with the flow fully developed. The wake structures are shown by the isosurfaces of $\lambda_2 = -2$ (Ref. 12) from our simulation. To ease the observation, color contours of crossflow velocity v/U are plotted in the (x, z)-plane at $y/D = 0$.

highest shedding frequency f_S behind the small cylinder, (2) L-cell vortex shed from the large cylinder with shedding frequency f_L, and (3) N-cell vortex with the lowest shedding frequency f_N located between the S- and L-cell regions. An illustration of these three vortex cells are shown in Fig. 1(b). According to Refs. 15 and 16, the average length of the N-cell vortex was found to decrease with increasing Re_D or decreasing D/d. Due to the different shedding frequencies of S-, N-, and L-cell vortices, complex vortex interactions and dislocations occurring between these three main vortex cells were observed and analyzed in Refs. 16–20. Similar spanwise vortex cells and the vortex interactions between them were also observed and investigated in the dual-step cylinder wakes.[21–23]

In addition to the three main spanwise vortex structures, the streamwise vortex system around the step surface has also been investigated in several previous studies.[14,24,25] In an experimental study of the flow around a single-step cylinder with $D/d = 2$ at $Re_D = 1100$, Dunn and Tavoularis[14] identified two kinds of streamwise vortices: a pair of *edge vortices* and a *junction vortex*. Edge vortices form around the leading edge of the step surface, while a *junction vortex* originates upstream of where the small cylinder interacts with the step surface. On the same side ($+Y$ or $-Y$ side) of the step cylinder, these two types of vortices rotate in opposite directions. Morton *et al.*[24] verified the existence of the *junction* and *edge vortices* in their numerical investigations at a slightly higher Reynolds number, $Re_D = 2000$. Besides, McClure *et al.*[25] and Ji *et al.*[26,27] reported the existence of a similar streamwise vortex system in flow around dual-step cylinders. McClure *et al.*[25] further concluded that the *junction vortex* primarily connects to the vortices shed from the large cylinder, while the *edge vortex* mainly connects to the small cylinder vortices. However, despite these well-verified findings, there still exist more flow details needed to be thoroughly described and investigated. For example; how different types of streamwise vortices develop in the flow around the step cylinder, how these vortices interact with each other, and whether other types of streamwise vortices exist around the step surface when Re_D increases.

Besides the step cylinder, the time-averaged streamwise vortex system has also been investigated in the wake of both surface-mounted finite circular and square cylinders. Sumner and Heseltine,[28] Sumner *et al.*,[29] and Zhang *et al.*[30] reported that a dipole type, a quadrupole type, or a six-vortices type appears depending on the aspect ratio and the Reynolds number of the surface-mounted cylinder. Moreover, near the free-end, Park and Lee,[31] Krajnovic,[32] and Hain *et al.*[33] observed a pair of streamwise tip vortices. By investigating the instantaneous and phase-averaged flow around surface-mounted cylinders, recent studies[34,35] suggested that the tip vortices are primarily caused by the deformed main spanwise vortices that connect back to the free end.

As mentioned before, $Re_D = 3900$ is a benchmark for the flow past a uniform circular cylinder, where there are many accurate numerical and experimental studies. However, until now, no one has investigated flow around a step cylinder at such Reynolds number. As a pioneer, the present study investigates the flow around a single-step cylinder with $D/d = 2$ at $Re_D = 3900$ by using direct numerical simulations (DNS). Our primary objectives are to investigate the formation mechanisms, vortex dynamics, and interactions between the vortices around the step position. Therefore, we restrict our analysis and discussions to the flow regions close to the step surface. Section II introduces the flow problem and the numerical methodology. In Sec. III, by analyzing the time-averaged flow, the vortex system around the step surface is described. In addition to the conventional *junction* and *edge vortices*, four other vortices are discussed. In Sec. IV, based on the instantaneous flow field, the formations of hair-pin vortices and Kelvin–Helmholtz vortices with an unexpectedly high shedding frequency are described.

II. NUMERICAL SIMULATIONS

A. Flow configuration

In the present study, we investigate the flow around a step cylinder as shown in Fig. 1(a). The uniform incoming flow U is in the positive x-direction. The side and top-down views of the flow domain are illustrated in Fig. 2. The streamwise length and the crossflow width of the computational domain are L_x and L_y. The inlet plane is located L_{x1} upstream from the center of the step cylinder, and the outlet plane is placed L_{x2} downstream. In the crossflow direction, the step cylinder is located in the middle of the domain. The spanwise height of the domain is L_z, where the length of the small and large cylinders occupy l and L, respectively. Detailed information of the flow domains used in the present study is summarized in Table I. Boundary conditions are as follows:

- The inlet boundary: uniform velocity profile $u = U$, $v = 0$, $w = 0$;
- The outlet boundary: Neumann boundary condition for velocity components ($\partial u/\partial x = \partial v/\partial x = \partial w/\partial x = 0$) and constant zero pressure condition (p=0);
- The other four sides of the computational domain: free-slip boundary conditions (For the two vertical sides: $v = 0$, $\partial u/\partial y = \partial w/\partial y = 0$, For the two horizontal sides: $w = 0$, $\partial u/\partial z = \partial v/\partial z = 0$);
- The step cylinder surfaces: no-slip and impermeable wall.

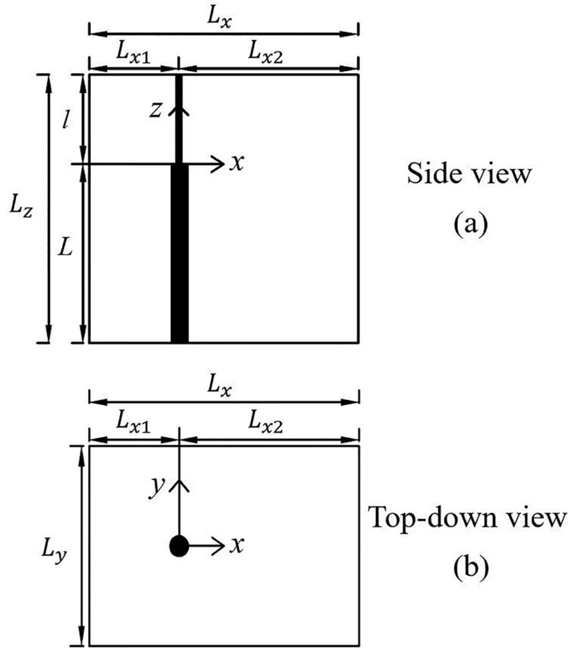

FIG. 2. Computational domain, origin, and coordinate system are illustrated from (a) side view and (b) top-down view.

B. Computational method

In this DNS study, the governing equations contain a mass conservation Eq. (1) and a time-dependent full three-dimensional incompressible Navier–Stokes Eq. (2):

$$\nabla \cdot \boldsymbol{u} = 0, \tag{1}$$

$$\frac{\partial \boldsymbol{u}}{\partial t} + (\boldsymbol{u} \cdot \nabla)\boldsymbol{u} = \nu \nabla^2 \boldsymbol{u} - \frac{1}{\rho}\nabla p, \tag{2}$$

where $\bigtriangledown$ is the Del operator, ν is the kinematic viscosity of the fluid, and ρ is the constant fluid density. For all simulations, a thoroughly validated finite-volume-based numerical code MGLET (Multi Grid Large Eddy Turbulence)[36,37] is used to directly solve the governing Eqs. (1) and (2) without introducing any turbulence model. In MGLET, Eqs. (1) and (2) are first discretized on a 3-D staggered Cartesian grid. Then, by using the midpoint approximation, the discretized equations are integrated over the surfaces of the discrete volumes. This leads to a second-order accuracy in space. In time, the discretized equations are integrated with Williamson's third-order low-storage Runge-Kutta scheme.[38] A constant time step Δt is used to ensure a CFL (Courant-Friedrichs-Lewy) number smaller than 0.5. The pressure corrections are achieved by using Stone's implicit procedure (SIP).[39]

The solid surface of the step cylinder is handled by an immersed boundary method (IBM). We use an unstructured triangular mesh to represent the surface of the geometry, and transfer information to IBM to block grid cells bounded by this surface. Detailed description and validation of this IBM can be found in Peller *et al.*[40] The computational domain is first divided into equal-sized cubic grid boxes, named the level-1 box. In each grid box, there are $N \times N \times N$ equal-sized cubic grid cells. For the region where complex flow phenomena appear, e.g., the regions close to the step cylinder and the region where vortices form, the grid boxes (the level-1 box) are equally divided into eight small cubic grid boxes, named the level-2 box. In every level-2 grid box, there are also $N \times N \times N$ grid cells. This means that the grid resolution in the level-2 box is two times finer than that in the level-1 box. This grid refinement-process goes on automatically until the finest grid level is reached. The grid structure in case Fine-B in the geometrical symmetry plane (the (x, z)-plane at $y/D = 0$) is plotted in Fig. 3 to schematically illustrate the grid structure.

Details of the mesh used in the simulations are summarized in Table I. Since all grid cells are cubic, the minimum grid cell size (Δ_c/D) is the same in x, y, and z directions. The four cases with the different minimum grid cell sizes (Δ_c/D), i.e., the Coarse, Medium, Fine-A and Very Fine cases, are set up for the grid study. In the geometry study, the mesh in the Fine-A case is also used with the cases Fine-B and Fine-C, in which the vertical lengths of the small (l) and large cylinder (L) parts are varied.

C. Grid convergence, spanwise length convergence, and statistical convergence

The detailed discussions about grid convergence, spanwise length convergence, and statistical convergence are provided in the Appendix. Based on the outcome of these considerations, we conclude that the mesh and configuration in the Fine-B case (see in Table I) are sufficiently good for reliable DNS simulations in this study. The statistical results obtained during the time period $tU/D = 350 - 850$ is sufficiently steady for the investigations in this study. All simulations were performed on an SGI (Silicon Graphics) ALTIX ICE X SLES—11sp3 cluster at NTNU. In the case Fine-B, there are six levels of grids

TABLE I. Detailed mesh and domain information of all simulations in this study. The case Coarse has five levels of grids, and the other cases all have six levels of grids. The cases Coarse, Medium, Fine-A, and Very Fine are used for the grid study. The cases, Fine-A, Fine-B, and Fine-C are used for the spanwise-length study. As shown in Fig. 3, the minimum grid cells (Δ_c/D) cover the region around the step cylinder.

Case	Min. cell size Δ_c/D	Time step $\Delta tU/D$	Domain size $(L_x \times L_y \times L_z)/D$	l / D	L / D	L_{x1}	L_{x2}	Number of grid cells ($\times 10^9$)
Coarse	0.010	0.0025	81.60 × 38.40 × 14.40	4.80	9.60	28.80	52.80	0.20
Medium	0.00625	0.0015	74.80 × 40.80 × 18.00	6.00	12.00	27.20	47.60	0.84
Fine-A	0.005	0.0012	81.60 × 38.40 × 14.40	4.80	9.60	28.80	52.80	1.21
Very Fine	0.004	0.0010	81.92 × 40.96 × 15.36	5.12	10.24	30.72	51.20	2.67
Fine-B	0.005	0.0012	81.60 × 38.40 × 24.00	9.60	14.40	28.80	52.80	2.02
Fine-C	0.005	0.0012	87.04 × 43.52 × 32.64	10.88	21.76	32.64	54.40	2.71

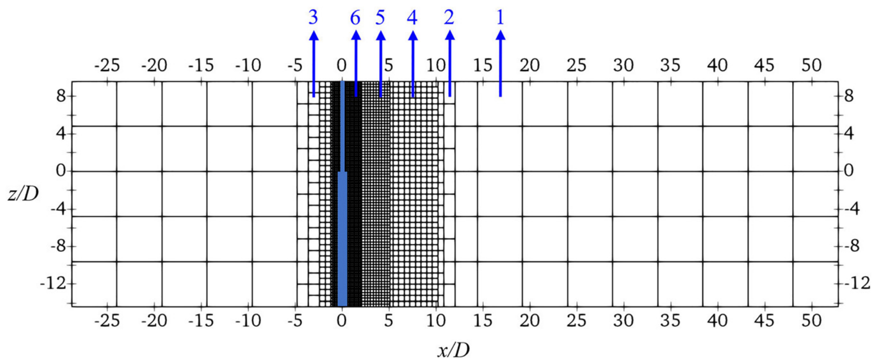

FIG. 3. An illustration of the multi-level grids in the (x, z)-plane at $y/D = 0$. Each square represents a slice of corresponding cubic Cartesian grid box that contains $N \times N \times N$ grid cells. Here, there are six levels of grid boxes as indicated by numbers. Owing to different minimum grid cell sizes, different cases studied in this study have either five or six levels of grid boxes.

containing in total 2.02×10^9 grid cells, with minimum grid cell size $\Delta_c/D = 0.005$. To run this case, we used 3360 processors (2 GB memory per processor) for at least 800 000 time steps. This single case consumed in total approximately 1.87 million CPU (central processing unit) hours. Recently, the same code MGLET has been used for simulations of wake flow behind other cylindrical structures at the same Reynolds number 3900 in Refs. 5, 41, and 42 where similar minimum grid cell size and CFL criteria were used.

III. TIME-AVERAGED FLOW AROUND THE STEP SURFACE

Similar to the flow around a finite-length cylinder,[28,30,35] the appearance of the time-averaged streamwise vortices is also a distinctive feature of the flow around the step surface of the step cylinder. In Fig. 4(a) by plotting the isosurfaces of time-averaged $\lambda_2 = -9$, a four horseshoe vortex system is identified in Fig. 4(a), where H1, H2, H3, and H4 are clear. Besides the conventional *junction vortex* (H1) and *edge vortex* (H3) reported in Refs. 14, 24, and 25, two new-observed vortices (H2 and H4) are identified. Figure 5(a) illustrates the evolution of these horseshoe vortices by projecting streamlines on several planes. To ease the observation, vortex cores [red lines in Fig. 5(a) and 5(b)] are calculated by using Tecplot post-processing software, which uses algorithms based on techniques outlined by Ref. 44. Additional information about the flow and vortices is shown in Fig. 5(b), where the vortex core lines and the limiting streamlines are projected on the step surface. Moreover, the time-averaged streamlines in the symmetry plane ($y/D = 0$) are plotted in Fig. 6(a) and 6(b). Based on Figs. 5 and 6(a), one can see that the main horseshoe vortex H1 is caused by both the leading edge separation and the impingement of the flow at the upstream surface of the step cylinder. When the flow approaches the step cylinder, an upward flow along the large cylinder is driven by the pressure difference between the stagnation pressure on the large cylinder and the pressure above the step surface at the same streamwise position. As the upward flow reaches the leading edge of the large cylinder, it separates and deflects to the incoming flow direction. After impinging the upstream surface of the small cylinder in the symmetry plane at the attachment saddle point A_1 (the blue dot at $z/D = 0.26$) in Fig. 6(a), a part of the flow is directed upward and some move downward. The majority of the downward flow attaches to the step surface at the attachment saddle point A_2 (the green dot at $x/D = -0.28$), and recirculates into the main horseshoe vortex H1. The other downward flow separates along the small cylinder wall at the separation saddle point S_1 (the red triangle at $z/D = 0.03$) and induces the formation of vortex H2. The formation of vortex H3 is caused by the separation of the backward flow beneath the vortex H1 on its way back to the leading edge of the large cylinder at the separation point S_2 (the red dot at $x/D = -0.42$). The corresponding local separation line is marked by the green dashed curve in Fig. 5(b). The neighboring H1 and H3 vortices are counter-rotating. Due to topological reasons, the vortex H4 appears upstream of H3 and rotates in the same direction as H1. As shown in Fig. 6(a), without formation of H4, the flow induced by the counterclockwise rotating vortex H3 would conflict with the incoming flow. Between the counter-rotating vortices H3 and H4, a reattachment saddle point A_3 is observed, as shown by the green triangle at

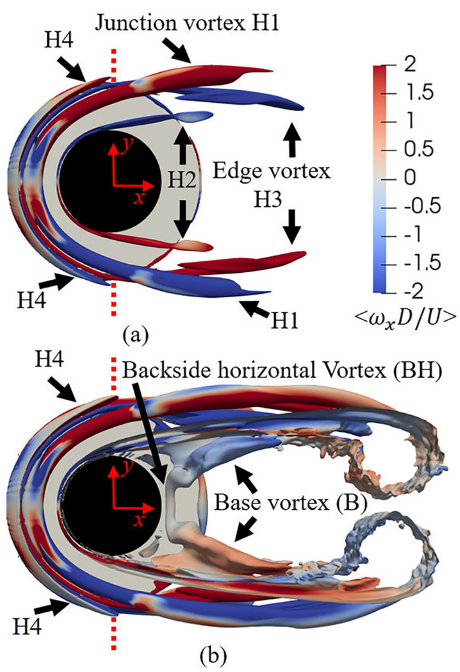

FIG. 4. (a) The time-averaged vortex structures around the step surface are illustrated by the isosurface of the time-averaged $\lambda_2 = -9$ at the top-down viewpoints colored by the time-averaged streamwise vorticity ω_x ($\omega_x = \partial w/\partial y - \partial v/\partial z$). (b) Same as (a) but $\lambda_2 = -0.2$. In (a) and (b), the main vortices around the step surface are indicated. The red dotted lines mark the position $x/D = 0$. (Note: The vortex structures in this paper were checked by plotting both the isosurfaces of λ_2 (Ref. 12) and Q (Ref. 43). No obvious difference was observed. To ease the presentation and discussion, only the isosurface of λ_2 is used.)

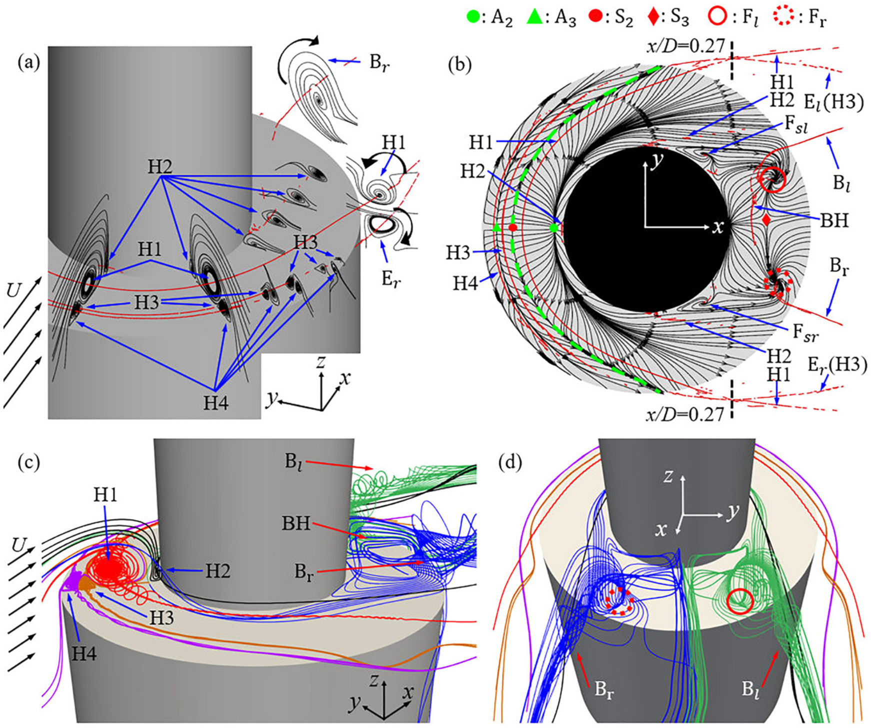

FIG. 5. (a) Time-averaged streamlines projected on several planes close to the step surface. The main vortex components are indicated. (b) Time-averaged streamlines projected on the step surface. The attachment saddle point A_2, the reattachment saddle point A_3, the separation saddle point S_2, a backside separation saddle point S_3, and two focal points F_l and F_r are marked by the green dot, green triangle, red dot, red diamond, red circle, and red dotted circle, respectively. The critical point for H1 and H3 is illustrated by two dashed black lines at $x/D = 0.27$. The local separation line is illustrated by a green dashed line in (b). In (a) and (b), the vortex core lines are plotted as red curves. (c) Three-dimensional flow evolution pattern with H1 in red, H2 in black, H3 in brown, H4 in purple, B_r in blue, and B_l in green. (d) Same as (c) but view from behind.

$x/D = -0.46$ in Fig. 6(a). In Figs. 5(c) and 5(d), the horseshoe vortices H1-H4 are illustrated by three-dimensional streamlines in different colors.

After these four horseshoe vortices (H1, H2, H3, and H4) form in front of the step cylinder, they wrap around the small cylinder and advect downstream. Based on Figs. 5(a) and 6(a), one can see that the conventional *edge vortex*[14,24] (E_r) rotates in the same direction as H3. Furthermore, the time-averaged isosurface of λ_2 in Fig. 4(a) and the instantaneous isosurface of λ_2 in Fig. 9(b) clearly show that as the horseshoe vortex H3 forms and wraps to the downstream, this vortex takes the role as the conventional *edge vortex*. However, this formation mechanism of the *edge vortex* (H3) is different from that reported by Dunn and Tavoularis.[14] They suggested that when the incoming flow is blocked by the small cylinder and pushed sideways by the rotating *junction vortex*, it spills over the edges of the step surface and rolls up into the *edge vortex*. However, Fig. 4 and 5 in this study clearly show

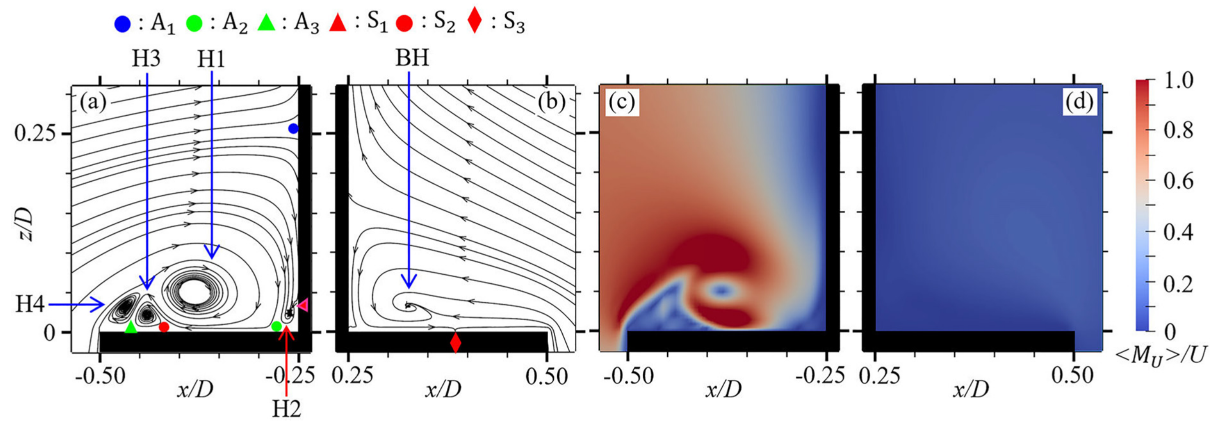

FIG. 6. (a) Time-averaged streamlines in a (x, z)-plane at $y/D = 0$ in the fore part of the step cylinder, the four horseshoe vortices (H1, H2, H3, and H4) are indicated. The same markers used in Fig. 5(a) are used here: the attachment saddle point A_2, the reattachment saddle point A_3, the separation saddle point S_2, a backside separation saddle point S_3 are marked by the green dot, green triangle, red dot, and red diamond, respectively. Moreover, an attachment saddle point A_1 and a separation saddle point S_1 are marked by a blue dot and red triangle, respectively. (b) Same as (a) but in the rear part of the step cylinder, the backside horizontal vortex (BH) is marked. (c) and (d) show the corresponding time-averaged magnitude of velocity $< M_U > /U$ contours in (a) and (b), respectively.

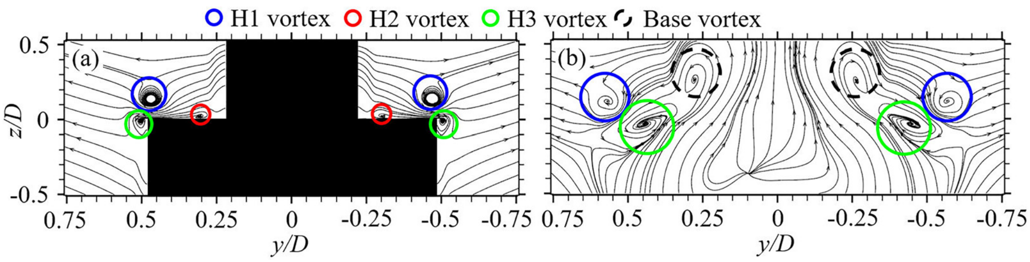

FIG. 7. (a) Time-averaged streamlines in a (*y*, *z*)-plane at $x/D = 0.1$. (b) Same as (a) but at $x/D = 0.7$. The horseshoe vortex H1, H2, and H3 and the *base vortex* are marked. Note: the slight asymmetry in (b) is caused by the marginal statistical time-sampling. The detailed discussion can be found in Appendix 3.

that the *edge vortex* is a horseshoe vortex caused by the local separation of the backward flow beneath the *junction vortex* H1. Indeed, both the junction and *edge vortex* are close to each other and the step surface, making it difficult to isolate them and investigate their formation mechanisms experimentally. Different from H1, H2, and H3 that extend relatively far into the wake flow ($x/D > 0.5$), H4 ends at $x/D \approx 0$. As shown in Figs. 4(a) and 4(b), when λ_2 changes from −9 to −0.2, H1, H2, and H3 extend further downstream and merge into mean recirculation wakes. However, H4 still ends around $x/D = 0$, as marked by the red dashed lines in Fig. 4(b). Further discussions about how H4 ends will be provided in Sec. IV.

Another obvious feature is the different developments of H1 and H3. Figure 5(b) clearly shows that for $x/D > 0$ the width of H1 gradually increases as moving to the downstream, while the width of H3 gradually decreases. The width here is referred to as the crossflow distance between the legs of the horseshoe vortex. Due to the different development tendencies, we define a critical position $x/D = 0.27$ for H1 and H3 as marked by the black dashed lines in Fig. 5(b). Upstream of it, the width of H3 is larger than that of H1. Downstream of it, the scenario is opposite. We find that it is the fact that H1 and H3 locate in different spanwise regions that causes their qualitatively different spatial evolution. As shown in Figs. 5(a), 6(a), and 7(a), when H1 and H3 wrap around the small cylinder and extend to $x/D = 0.1$, H1 is still located above the step surface ($z/D > 0$), while H3 already extends outside and below the step surface ($z/D < 0$). In Fig. 8, in comparison, the time-averaged streamlines behind the small and large cylinder are plotted in the (*x*, *y*)-planes at $z/D = 0.1$ and $z/D = -0.05$. The vortex core lines of H1, H2, and H3 are also projected in these planes. One can see that around the small cylinder, at $0 < x/D < 0.75$, the incoming flow has an outward flow direction.

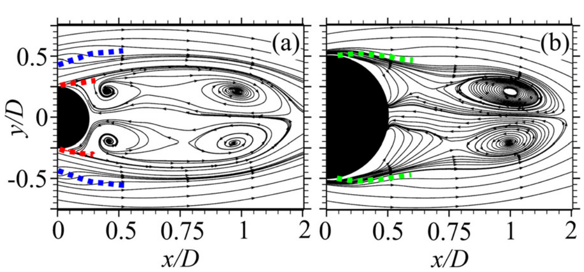

FIG. 8. (a) Time-averaged streamlines in a (*x*, *y*)-plane at $z/D = -0.1$. (b) Same as (a) but at $z/D = 0.05$. The vortex core lines corresponding to H1, H2, and H3 are projected in (a) and (b) by the blue, red and green dotted lines, respectively.

The width of the recirculation region gradually increases. On the contrary, behind the large cylinder part, the incoming flow has an inward flow direction at $0 < x/D < 0.75$. According to these different flow directions, from $x/D = 0.1$ to $x/D = 0.7$, the width of H1 increases from 0.98*D* in Fig. 7(a) to 1.15*D* Fig. 7(b), while the width of H3 decreases from 1.00*D* to 0.90*D*. Moreover, due to the same reason, the width of H2 also slightly increases as it extends downstream above the step surface, as shown in Figs. 5(b) and 6(a). At a spanwise position far away from the step surface, due to the diameter ratio, the wake width behind the small cylinder is smaller than that behind the large cylinder. Close to the step surface, however, for the wakes behind the small and large cylinders to smoothly connect with each other, the flow behaves differently behind the small and the large cylinders. A similar four-horseshoe vortex system has also been reported in flow past a wall-mounted cylinder,[45–47] but never been observed before in the flow around a step cylinder. Moreover, the newly observed opposite tendencies of crossflow widths of the horseshoe vortices are unique. The behavior of the crossflow width is normally the same for different vortex components of a horseshoe vortex system in the near wake of flow around wall-mounted cylinders.

In addition to these four characteristic horseshoe vortices, we capture a pair of counter-rotating *base vortices* (B_r and B_l) generated from two focal points F_r and F_l on the step surface behind the small cylinder, as shown in Fig. 5(b). Between them, another backside horizontal vortex (BH) is identified. Although similar focal points and vortex structures have been reported in the flow around a wall-mounted cylinder,[48–50] it is surprising to observe the formation of these vortices in such a narrow step surface with only 0.25*D* radial width. Figure 5(b) and 6(b) show that when the back-flow caused by the recirculations reaches the trailing edge of the large cylinder in the (*x*, *z*)-plane at $y/D = 0$, vortex BH forms in the same way as H1 does, as explained in the previous paragraph. The corresponding backside separation saddle point is marked by the red diamond in Figs. 5(b) and 6(b). Moreover, Figs. 6(c) and 6(d) show that the strength of the back-flow is much weaker than that of the incoming flow. Consequently, different from the incoming flow that induces four vortices (H1, H2, H3, and H4) in the forepart of the step surface, the weak back-flow only induces one backside horizontal vortex (BH) on the rear part of the step surface. Additionally, when the recirculation flow behind the small cylinder reaches the two focal points F_r and F_l on the step surface, it spirals upward and moves into the positive $x-$direction to form a pair of *base vortices* (B_r and B_l), as indicated in Figs. 5(c) and 5(d). The corresponding swirls caused by these *base vortices* are seen in the (*y*, *z*)-plane at $x/D = 0.7$ in Fig. 7(b), as highlighted by the black

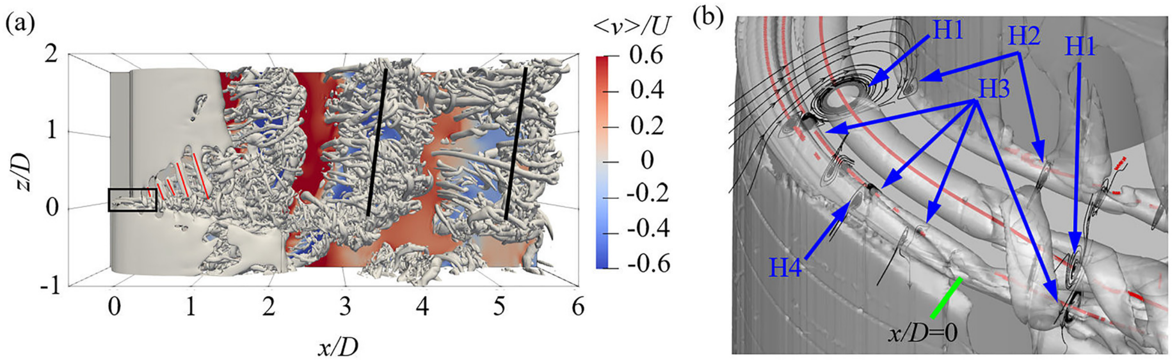

FIG. 9. (a) Instantaneous isosurface of $\lambda_2 = -2$ together with color contours of crossflow velocity v/U in the (x, z)-plane at $y/D = 0$. The Kelvin–Helmholtz vortex and the S-cell vortex are marked by the red and black lines, respectively. (b) A zoomed-in view of the step region (black rectangle) in (a). The streamwise position $x/D = 0$ is marked by a short green line.

dashed circles. Due to the modest strength of the recirculation flow, the backside horizontal vortex (BH) and the pair of *base vortices* (B_r and B_l) are weaker compared to the horseshoe vortices. We can only observe four horseshoe vortices in the isosurface plot of $\lambda_2 = -9$ in Fig. 4(a). BH, B_r, and B_l become visible only in the isosurface plot of $\lambda_2 = -0.2$. Moreover, the colors of the streamwise vorticity ω_x on the isosurfaces of B_r and B_l are obviously lighter than those of H1 and H3. These facts confirm the weaker of BH, B_r, and B_l.

IV. INSTANTANEOUS FLOW AROUND THE STEP SURFACE

The instantaneous isosurface of λ_2 is presented in the step region in Figs. 9 and 10. The boundary layer is laminar in the fore part of the step cylinder, therefore the four horseshoe vortices seen in the time-averaged flow field are also clearly observed in the instantaneous flow field at $x/D < 0$. On the other hand, the vortex structures corresponding to BH, B_r, and B_l are difficult to identify in the instantaneous flow. These vortices are located in the turbulent wake of the small cylinder, which makes them indistinguishable in the small turbulent eddies. For $x/D > 0$, complex vortex interactions and small turbulent eddies appear. Two instantaneous features are remarkable: the formation of hairpin vortices between the horseshoe vortices, and the formation of secondary spanwise vortices close to the rear part of the small cylinder.

By plotting iso-surfaces of $\lambda_2 = -0.2$ at six consecutive time instants in Fig. 10, two stages are identified in the formation process of the hairpin vortices: the initial stage [from Figs. 10(a)–10(c)] and the developed stage [in Figs. 10(d)–10(f)] which are marked by the red and black colors, respectively. Unlike the hairpin vortex structures that form between two counter-rotating streamwise vortices located on different sides of the obstacle structures,[51,52] in this study, the hairpin vortex forms between the legs of two counter-rotating vortices H1 and H3 on the same side of the step cylinder. Additionally, before the hairpin vortex forms, a special vortex bridge appears between two co-rotating vortices H1 and H4. This stage is referred to as the initial stage. From Figs. 10(a)–10(c), as H4 extends from $x/D = 0$ to $x/D \approx 0.12$ a vortex bridge gradually forms between H1 and H4 as marked by a black circle. In Fig. 10(d), when the vortex bridge separates from H4 and reconnects to H3, a hairpin vortex forms between two counter-rotating vortices H1 and H3, as indicated by the black dotted curve. In parallel, H4 shrinks back to $x/D = 0$, which explains the fact that the time-averaged H4 ends at $x/D \approx 0$ in Fig. 4, as mentioned in Sec. III. At the developed stage, from Figs. 10(d)–10(e), just in front of the hairpin vortex marked by the black dashed curve, two additional

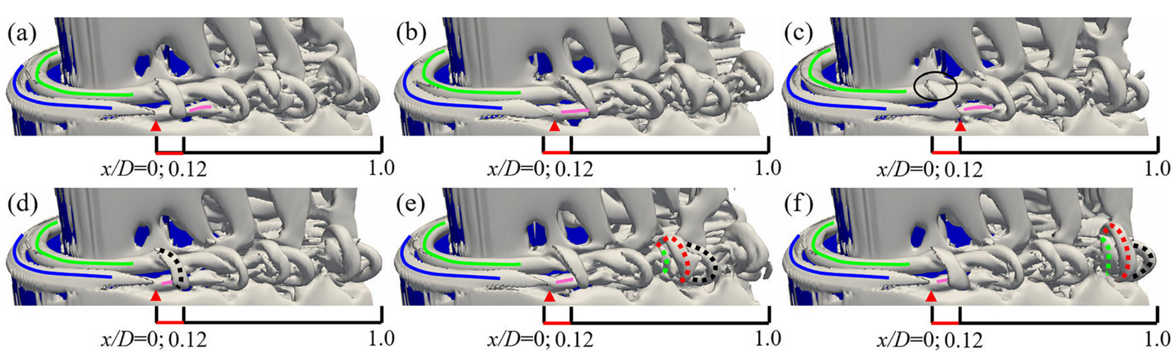

FIG. 10. Consecutive instantaneous isosurfaces of $\lambda_2 = -0.2$ showing developments of vortex structures around the step position in the $Re_D = 3900$ case. The vortices H1, H3, and H4 are marked by the green, pink and blue lines, respectively. (a) $tU/D = 860.052$, (b) $tU/D = 860.172$, (c) $tU/D = 860.292$, (d) $tU/D = 860.364$, (e) $tU/D = 861.060$, and (f) $tU/D = 861.300$. The end position of H4 (the blue curve) is marked by the red triangle. The corresponding animation can be found in the supplementary file.

hairpin vortices form, as indicated by the red and green dashed curves. These three hairpin vortices nest together to form a hairpin vortex group. From Figs. 10(e)–10(f), this vortex group convects downstream from $x/D \approx 0.7$ to $x/D \approx 1$. To clearly show the formation process of the hairpin vortices, we upload an animation to the supplementary material, from which one can clearly see that, in every vortex group, two or three hairpin vortices form in every $0.3D/U$.

Another remarkable instantaneous phenomenon is the secondary spanwise vortices as highlighted by the red lines in Fig. 9(a). These vortices, similar to those caused by the Kelvin–Helmholtz (KH) instability, are formed before the main spanwise S-cell vortices [the black lines in Fig. 9(a)] shed from the small cylinder. A pair of corresponding spiral flows (F_{sr} and F_{sl}) are clearly captured in the time-averaged streamlines on the step surface in Fig. 5(b). The frequency of conventional KH vortices[53,54] follows:

$$f_{KH}/f_K = 0.0235 \times Re^{0.67}, \tag{3}$$

in which f_{KH} and f_K represent the shedding frequency of the KH vortex and the corresponding main Karman vortex, respectively. The main Karman vortex behind the small cylinder in this study is referred to as f_S in Fig. 11. The ratio between the KH and main Karman vortices in this study (i.e., f_{KH}/f_S=1.6/0.2 $\approx$ 8) is two times higher than the empirical value from Eq. (3) (i.e., $0.0235 \times 1950^{0.67} \approx 4$ where Re_d instead of Re_D is used because the focused KH vortex appears behind the small cylinder). The conventional KH vortex is caused by the KH instability, which amplifies the convection of perturbations in the shear layer. According to the previous study by Robinson,[55] in which flow along a solid wall was considered, the formation of the hairpin vortices was observed to help promote convection of velocity perturbations from the wall to the flow in the upper region. Figure 12 shows that closer to the group of hairpin vortices the velocity fluctuation clearly becomes stronger in the region where KH vortices form. This implies that the KH vortex in this study is caused by the combined effects of both the KH instability and the instability transported by the horseshoe vortex. This causes the unexpectedly high shedding frequency f_{KH}.

V. CONCLUSIONS

In this study, we use DNS to investigate both the time-averaged and instantaneous flow fields around the step cylinder with $D/d = 2$ at $Re_D = 3900$. In general, our results show good agreement with previous studies[14,24–26] with respect to the formation of the *junction* and *edge vortices* around the step surface of the step cylinder. Moreover, similar *base vortices* identified in the flow past a wall-mounted cylinder by Refs. 48–50 are also captured in the rear part of the step surface. Furthermore, our numerical results provide more complete and detailed information about the flow around the step surface.

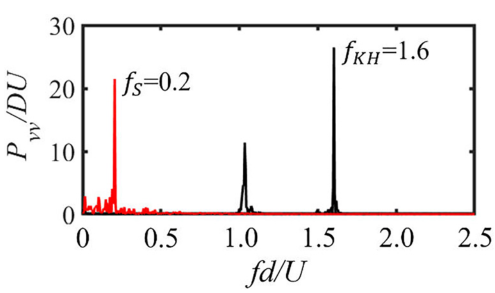

FIG. 11. Crossflow velocity (v) spectra at positions $(x/D, y/D, z/D)$ = (0.53, 0.4, 0.2) and (3, 0.6, 0.2) are plotted in black and red, respectively. The frequency components corresponding to f_S and f_{KH} are marked. Note that the frequency is nondimensionalized based on the small cylinder's diameter (d). (The value of f_{KH} can also be measured from the movie in the supplementary material.)

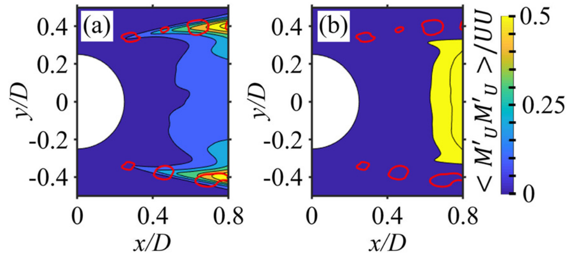

FIG. 12. (a) Contours of time-averaged magnitude velocity fluctuation $< M'_U M'_U > /UU$ plots in a horizontal plane at $z/D = 0.2$, together with instantaneous contours of $\lambda_2 = -9$ at $tU/D = 860.36$ plot in red color; (b) Same as (a) but at $z/D = 3$. The same instantaneous contours of $\lambda_2 = -9$ in (a) are directly projected in (b).

The time-averaged iso-surfaces of λ_2 and time-averaged streamlines show that, due to the flow impingement, flow recirculation and flow separations on the junction surfaces between the root of the small cylinder and the step surface, four horseshoe vortices (H1, H2, H3, and H4) form above the step surface in front of the upper small cylinder. In addition to the conventional *junction vortex* (H1) and the *edge vortex* (H3), two additional horseshoe vortices H2 and H4 are clearly identified. The resulting four horseshoe vortex system is therefore identified. Under the influence of the different flow behaviors in the wakes of the small and large cylinders, the H1, H2, and H3 vortices develop differently. When they reach $x/D > 0$ and extend downstream, the crossflow widths of H1 and H2 continue to increase; however, the crossflow width of H3 decreases. Consequently, a critical point for H1 and H3 is defined. Moreover, in the rear part of the step surface ($x/D > 0$), we capture a pair of *base vortices* (B_r and B_l) and a backside horizontal vortex (BH).

By detailed investigations of the instantaneous flow, we find that the four horseshoe vortices clearly exist in both the time-averaged and instantaneous flow field. In the forepart of the step surface ($x/D < 0$), the vortices H1, H2, H3, and H4 are quite stable and only slightly fluctuate in time. On the other hand, vortices B_r, B_l, and BH are difficult to identify in the instantaneous flow due to their weak strength. As H4 extends to $x/D > 0$, a vortex bridge gradually forms between the legs of two co-rotating horseshoe vortices H1 and H4. After this vortex bridge separates from the end of H4 at $x/D \approx 0.12$, a hairpin vortex forms between the legs of two counter-rotating horseshoe vortices H1 and H3 located on the same side of the step cylinder. In the neighboring region upstream of this hairpin vortex, either one or two more hairpin vortices form before convecting to the wake region dominated by small turbulent eddies. Another remarkable phenomenon is the appearance of Kelvin–Helmholtz (KH) vortices with an unexpectedly high shedding frequency behind the small cylinder. Our results suggest that their appearances are caused by the combined effects of both the KH instability and the instability transported by the horseshoe vortices.

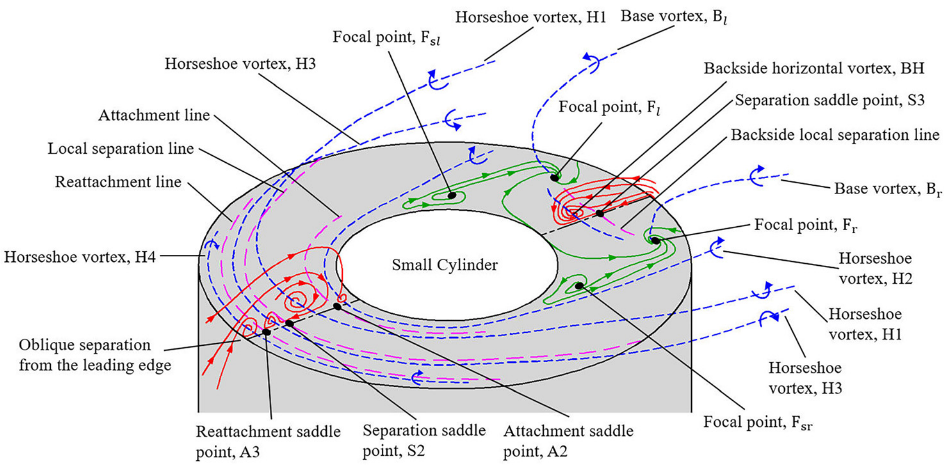

FIG. 13. Schematic of the flow field for the single-step cylinder with $D/d = 2$ at $Re_D = 3900$ showing the main flow features. To ease observations, the surface of the small cylinder is omitted.

Based on the discussions in this paper, an overall schematic of the flow around the step surface of the step cylinder with $D/d = 2$ at $Re_D = 3900$ is illustrated in Fig. 13, where the main time-averaged vortex structures and flow features are identified. To ease observations, the geometry of the small cylinder is omitted.

SUPPLEMENTARY MATERIAL

See the supplementary material for movie files.

ACKNOWLEDGMENTS

Computing resources were granted by the Norwegian Research Council (Program for Supercomputing) under project nn9191k. The first author would like to thank China Scholarship Council (CSC) for financial support.

APPENDIX: GRID CONVERGENCE, SPANWISE LENGTH CONVERGENCE, AND STATISTICAL CONVERGENCE

This study focuses on the flow around the step surface of the step cylinder. Therefore, in this section, we execute the convergence tests in the region close to the step surface, i.e., the S- and N-cell regions [see in Fig. 1(b)].

TABLE II. Strouhal numbers of the two dominating vortex cells (S-cell, $St_S = f_S D/U$, and N-cell, $St_N = f_N D/U$) are shown in the second and third columns. They are obtained by means of a discrete Fourier transform (DFT) of continuous velocity data along a vertical sampling line with density 0.01D parallel to the $z-$axis at position (x/D, y/D) = (2.02, 0), over at least 300 time units (D/U). In the last two columns, the time-averaged drag force coefficients are calculated by using Eq. (A1). Subscript S stands for the small cylinder part $1 < z/D < 4$, N stands for the large cylinder part in the N-cell region $-4 < z/D < -1$.

Case	St_S	St_N	$\overline{C_{DS}}$	$\overline{C_{DN}}$
Coarse	0.42	0.18	1.02	0.87
Medium	0.42	0.19	0.97	0.86
Fine-A	0.43	0.19	0.95	0.85
Very fine	0.44	0.19	0.94	0.85

1. Grid convergence

Table II shows the Strouhal number (St) and the time-averaged drag coefficient ($\overline{C_D}$) obtained in the S- and N-cell regions. In these two regions, we capture two dominating frequencies St_S and St_N, corresponding to the shedding frequencies of the main S- and N-cell vortices. The time-averaged drag coefficient is normalized as

$$\overline{C_{Dj}} = \frac{\overline{F_{xj}}}{0.5\rho A_j U^2}, \quad j = S, N, \tag{A1}$$

where the subscript S represents the small cylinder part covered by the S-cell vortex at $1 < z/D < 4$, and N represents the large cylinder part covered by the N-cell vortex at $-4 < z/D < -1$. A_j is the projected areas of the different parts in the (y, z)-plane. One can easily calculate: $A_S/D^2 = 1.5$, and $A_N/D^2 = 3$. When the mesh is refined from the case Coarse to Very Fine, the data in Table II shows converging trends of all quantities listed. Moreover, in Fig. 14, we plot the time-averaged streamwise velocity $< u > /U$ and the time-averaged pressure coefficient ($< C_P >$) along a vertical sampling line located at (x/D, y/D) = (2.02, 0). $< C_P >$ is defined as

$$< C_P >= \frac{< P > -P_0}{0.5\rho U^2}, \tag{A2}$$

where $< P >$ is the time-averaged pressure along the sampling line and P_0 is the pressure at the inlet boundary. The curves in Fig. 14 clearly show a converging tendency from the Coarse case to the Very Fine case. Especially in the region ($-5 < z/D < 3$) close to the step position ($z/D = 0$), we barely see any difference between the Fine-A and Very Fine cases.

2. Spanwise length convergence

Due to the large number of grid cells and the smaller time step, the computational cost of the Very Fine case is significantly higher than that of the Fine-A case. Therefore, in the spanwise length convergence test, we built Fine-B and Fine-C by using the same grid structures in Fine-A, and changed the lengths of both the small (l) and large cylinder (L) cylinders (see in Table I).

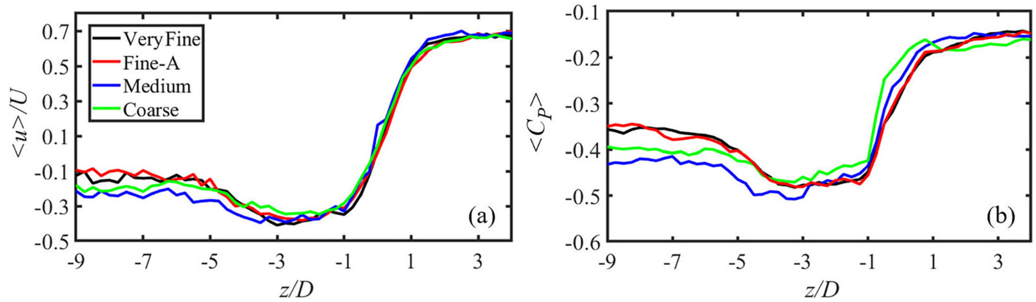

FIG. 14. (a) Distribution of time-averaged streamwise velocity ($< u > /U$) along a sampling line at (x/D, y/D) = (2.02, 0) in the Coarse, Medium, Fine-A, and Very Fine cases. (b) Same as (a) but for the time-averaged pressure coefficient ($< C_P > /U$).

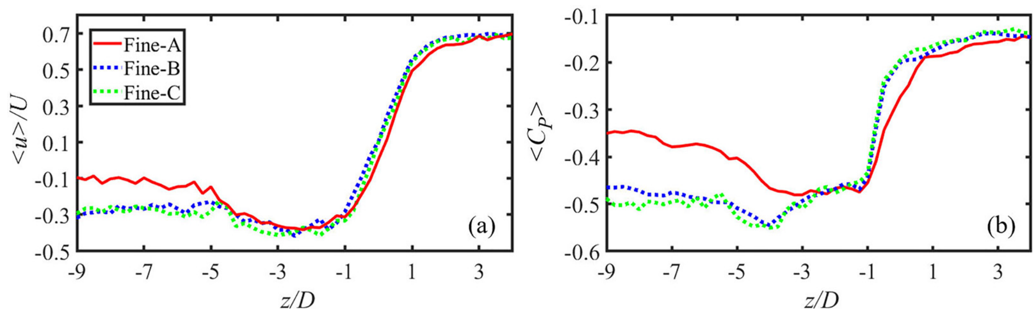

FIG. 15. (a) Distribution of time-averaged streamwise velocity ($< u > /U$) along a sampling line at (x/D, y/D) = (2.02, 0) in the Fine-A, Fine-B, and Fine-C cases. (b) Same as (a) but for the time-averaged pressure coefficient ($< C_P > /U$).

Figure 15 shows the distributions of $< u > /U$ and $< C_P >$ along a vertical sampling line at (x/D, y/D) = (2.02, 0) in the Fine-A, Fine-B, and Fine-C cases. The results show that the free-slip wall boundary condition at the top and bottom of the domain have relatively strong influences on the results in the Fine-A case. Especially at $z/D = -9$ which is close to the bottom boundary ($z/D = -9.6$) in Fine-A, $< u > /U$ and $< C_P >$ in Fine-A are only one-third and half of those in Fine-B and Fine-C, respectively. On the other hand, the difference between the blue (Fine-B) and green (Fine-C) dotted curves is very small, especially in the region around the step position at $-5 < z/D < 3$. Furthermore, in Fig. 16, we plot the time-averaged streamwise vorticity $< \omega_x > D/U$ contours and the time-averaged λ_2 contours in a (y, z)-plane at $x/D = 0.3$, which is in the step area just behind the small cylinder. The results of Fine-A show obvious differences when comparing with the results of Fine-B and Fine-C. On the other hand, the difference between results of

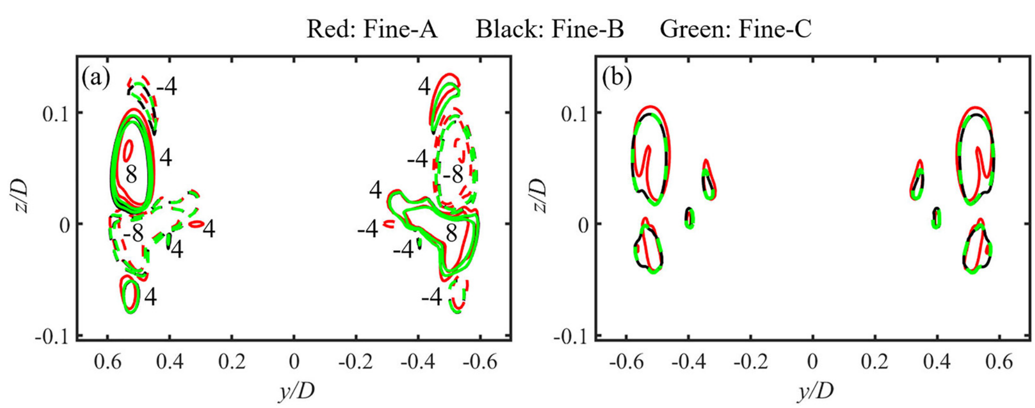

FIG. 16. (a) Contours of time-averaged streamwise vorticity $< \omega_x > D/U = \pm 4$ and ± 8 plotted in a (y, z)-plane at $x/D = 0.3$. Solid and dashed lines represent positive and negative values. (b) Contours of time-averaged $\lambda_2 = -9$ (Ref. 12) plotted in the same plane used in (a).

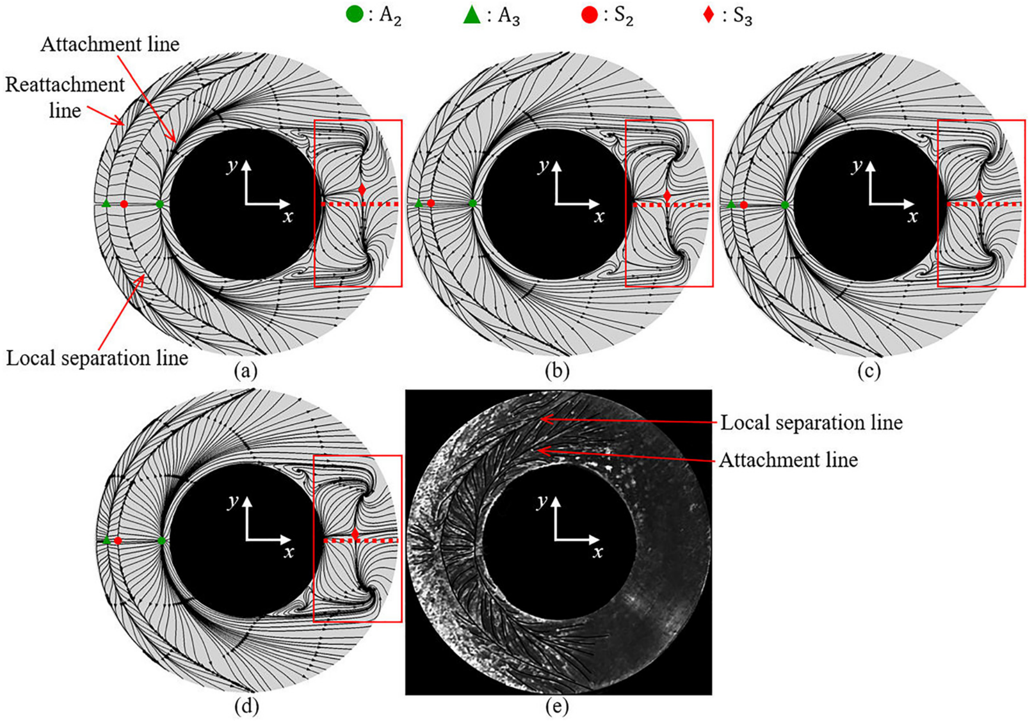

FIG. 17. (a) Time-averaged streamlines projected on the step surface based on the velocity data in the time range $tU/D = 350 - 650$. (b) Same as (a) but based on the velocity data within $tU/D = 350 - 850$. (c) Same as (a) but based on the velocity data within $tU/D = 350 - 950$. (d) Same as (a) but based on the velocity data within $tU/D = 650 - 950$. (e) Hydrogen bubble surface visualization on the step junction of a dual-step cylinder for $Re_D = 2100$, $D/d = 2$ from Morton and Yarusevych.[56] The attachment saddle point A_2, the reattachment saddle point A_3, the separation saddle point S_2, and the backside separation saddle point S_3 are marked by the green dot, green triangle, red dot, and red diamond, respectively.

Fine-B (the black curves) and Fine-C (the green curves) is negligible. The overlap between the green and black curves proves that the spanwise length in Fine-B and Fine-C cases converge well in the flow field close to the step surface.

3. Statistical convergence

The discussions in Secs. III and IV are based on both the instantaneous and time-averaged flows, therefore a careful examination of the statistical convergence is necessary. We first simulated case Fine-B for 350 time units (D/U) to ensure that the flow is properly developed. Then the time-averaged streamlines on the step surface are calculated based on the velocity data with three different sampling times: tU/D from 350 to 650 in Fig. 17(a), tU/D from 350 to 850 in Fig. 17(b), and tU/D from 350 to 950 in Fig. 17(c). Similar time-averaged flow fields are shown in the upstream part of the step surface (i.e., $x/D < 0$), where an attachment line, a reattachment line, and one separation line are indicated. The detailed formation mechanisms of these three special lines are described in Sec. III. At their intersection points with the $x-$axis, the corresponding attachment saddle point A_2, reattachment saddle point A_3, and separation saddle point S_2 are marked in Fig. 17. To describe the position of the attachment, reattachment, and separation lines, we define the position of their corresponding saddle points as their own position. Based on Fig. 17 and Table III, one can easily see that the variation tendencies of these three lines are similar. Moreover, the position of the attachment and reattachment lines keep constant in all three subplots in Fig. 17. Only the location of the local separation line moves $0.02D$ upstream from Figs. 17(a)–17(b), then remains unchanged from Figs. 17(b) and 17(c). Moreover, in Fig. 17(d), the

TABLE III. Location of singular points for different sampling periods.

Time period (tU / D)	A_2 (x / D, y / D)	A_3 (x / D, y / D)	S_2 (x / D, y / D)	S_3 (x / D, y / D)
350–650	(−0.28, 0)	(−0.46, 0)	(−0.40, 0)	(0.38, 0.05)
350–850	(−0.28, 0)	(−0.46, 0)	(−0.42, 0)	(0.36, 0.03)
350–950	(−0.28, 0)	(−0.46, 0)	(−0.42, 0)	(0.36, 0.02)
650–950	(−0.28, 0)	(−0.46, 0)	(−0.43, 0)	(0.36, 0.02)

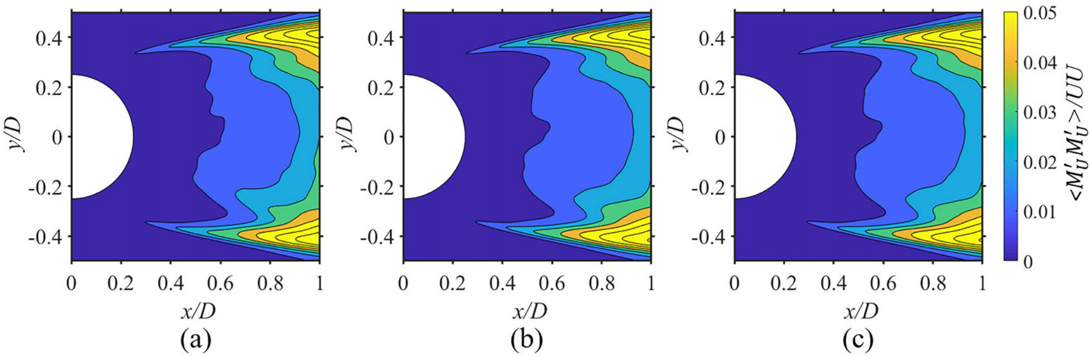

FIG. 18. (a) Contours of time-averaged magnitude velocity fluctuation ($< M'_U M'_U > /UU$) plots in a horizontal plane at $z/D = 0.2$ based on the velocity data $tU/D = 350$–650. (b) Same as (a) but based on the velocity data $tU/D = 350$–850. (c) Same as (a) but based on the velocity data $tU/D = 350$–950.

time-averaged streamlines are plotted based on the velocity data within $tU/D = 650$–950. The negligible difference between Figs. 17(c) and 17(d) proves that no temporal feature appears after $tU/D = 650$. Morton and Yarusevych[56] used the hydrogen bubble technique to illustrate the flow on the step surface of a dual-step cylinder with $D/d = 2$ at $Re_D = 2100$, as shown in Fig. 17(e). Although the configuration and the Reynolds number are not the same as in this paper, both the attachment line and the local separation line are similar and clear in their study and ours.

The second-order statistical convergence is also checked. In Fig. 18, the contours of time-averaged magnitude velocity fluctuations $< M'_U M'_U > /UU$ are plotted in a horizontal plane at $z/D = 0.2$, based on three different time periods. Based on the same time periods, Figs. 19(a) and 19(b) show the time-averaged Reynolds shear stress $< u'v' > /UU$ at $(x/D, z/D) = (1, 7)$ and $(x/D, z/D) = (2, -14)$, respectively. Both Figs. 18 and 19 indicate that the differences in the 2nd order velocity fluctuations between the time periods $tU/D = 350$–850 and $tU/D = 350$–950 are negligible.

Considering that the step cylinder configuration used in this study is symmetric about the $x-z$ coordinate surface, under the uniform incoming flow in the $x-$direction, the time-averaged wake flow is also expected to be symmetric about the $x-$axis. However, as highlighted by the red rectangle in Fig. 17, an unexpected asymmetry appears on the rear part of the step surface at $x/D > 0$, where a separation saddle point is marked by a red diamond. The cross-flow distance between the red diamond and the center red dotted line ($y/D = 0$) can reflect the strength of the asymmetry. As shown in Fig. 17 and Table III, the red diamond continuously moves closer to the center red dotted line ($y/D = 0$) as the simulation time increases, i.e., the strength of the asymmetry in wake flow continues to decrease with increasing simulation time length. If the simulation time further increases, a symmetric wake flow can be expected, where the red diamond will locate exactly on the center red dotted line. However, we think it is too time-consuming and unnecessary to run the simulation even longer just to obtain a completely symmetric time-averaged wake. Because first the asymmetry in Figs. 17(b) and 17(c) are already weak, the red diamond only deflects

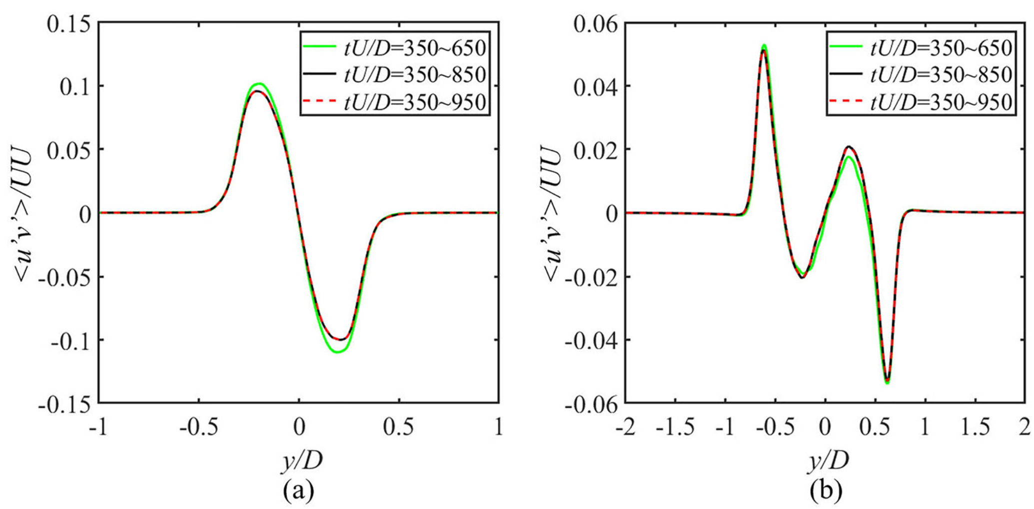

FIG. 19. (a) Co-variance of the velocity fluctuations ($< u'v' > /UU$) at $(x/D, z/D) = (1, 7)$. (b) Same as (a) but at $(x/D, z/D) = (2, -14)$.

$0.02 - 0.03D$ away from the centerline. And more importantly, this small asymmetry has no effect on our discussions in this study.

In general, based on the results presented in this section, we conclude that the mesh and configuration in the Fine-B case (see Table I) are sufficiently good for reliable DNS simulations in this study. The statistical results obtained during both time periods $tU/D = 350 - 850$ and $tU/D = 350 - 950$ are sufficiently converged for the investigations in this study.

DATA AVAILABILITY STATEMENT

The data that support the findings of this study are available from the corresponding author upon request.

REFERENCES

[1] C. H. K. Williamson, "Vortex dynamics in the cylinder wake," Annu. Rev. Fluid Mech. **28**, 477–539 (1996).

[2] B. Sumer and J. Fredsøe, *Hydrodynamics around Cylindrical Structures* (World Scientific, Singapore, 1997), Vol. 26.

[3] O. Lehmkuhl, I. Rodríguez, R. Borrell, and A. Oliva, "Low-frequency unsteadiness in the vortex formation region of a circular cylinder," Phys. Fluids **25**, 085109 (2013).

[4] B. N. Rajani, A. Kandasamy, and S. Majumdar, "LES of flow past circular cylinder at Re= 3900," J. Appl. Fluid Mech. **9**, 1421–1435 (2016).

[5] H. Strandenes, B. Pettersen, H. I. Andersson, and M. Manhart, "Influence of spanwise no-slip boundary conditions on the flow around a cylinder," Comput. Fluids **156**, 48–57 (2017).

[6] G. Tian and Z. Xiao, "New insight on large-eddy simulation of flow past a circular cylinder at subcritical Reynolds number 3900," AIP Adv. **10**, 085321 (2020).

[7] P. Parnaudeau, J. Carlier, D. Heitz, and E. Lamballais, "Experimental and numerical studies of the flow over a circular cylinder at Reynolds number 3900," Phys. Fluids **20**, 085101 (2008).

[8] V. M. Molochnikov, N. I. Mikheev, A. N. Mikheev, A. A. Paereliy, N. S. Dushin, and O. A. Dushina, "SIV measurements of flow structure in the near wake of a circular cylinder at Re= 3900," Fluid Dyn. Res. **51**, 055505 (2019).

[9] S. Rodriguez and J. Jaworski, "Strongly-coupled aeroelastic free-vortex wake framework for floating offshore wind turbine rotors. Part 2: Application," Renewable Energy **149**, 1018–1032 (2020).

[10] A. Felisita, O. Gudmestad, D. Karunakaran, and L. Martinsen, "Review of steel lazy wave riser concepts for the North Sea," J. Offshore Mech. Arct. Eng. **139**, 011702 (2017).

[11] D. Yin, H. Lie, and J. Wu, "Structural and hydrodynamic aspects of steel lazy wave riser in deepwater," J. Offshore Mech. Arct. Eng. **142**, 020801 (2020).

[12] J. Jeong and F. Hussain, "On the identification of a vortex," J. Fluid Mech. **285**, 69–94 (1995).

[13] C. G. Lewis and M. Gharib, "An exploration of the wake three dimensionalities caused by a local discontinuity in cylinder diameter," Phys. Fluids A **4**, 104–117 (1992).

[14] W. Dunn and S. Tavoularis, "Experimental studies of vortices shed from cylinders with a step-change in diameter," J. Fluid Mech. **555**, 409–437 (2006).

[15] C. Norberg, "An experimental study of the flow around cylinders joined with a step in diameter," in *Proceedings of the 11th Australasian Fluid Mechanics Conference*, *Hobart, Australia* (University of Tasmania, Australia, 1992), Vol. 1, pp. 507–510.

[16] C. Tian, F. Jiang, B. Pettersen, and H. I. Andersson, "Diameter ratio effects in the wake flow of single step cylinders," Phys. Fluids **32**, 093603 (2020).

[17] C. Morton and S. Yarusevych, "Vortex shedding in the wake of a step cylinder," Phys. Fluids **22**, 083602 (2010).

[18] C. Tian, F. Jiang, B. Pettersen, and H. I. Andersson, "Antisymmetric vortex interactions in the wake behind a step cylinder," Phys. Fluids **29**, 101704 (2017).

[19] C. Tian, F. Jiang, B. Pettersen, and, and H. I. Andersson, "The long periodicity of vortex dislocations in the wake behind a step cylinder," in *Proceedings of 10th National Conference on Computational Mechanics*, *Trondheim, Norway*, June 3–4 (2019) pp. 81–99 (CIMNE, Barcelona, Spain, 2019).

[20] C. Tian, F. Jiang, B. Pettersen, and H. I. Andersson, "Vortex dislocation mechanisms in the near wake of a step cylinder," J. Fluid Mech. **891**, A24 (2020).

[21] C. Morton, S. Yarusevych, and F. Scarano, "A tomographic particle image velocimetry investigation of the flow development over dual step cylinders," Phys. Fluids **28**, 025104 (2016).

[22] C. Morton and S. Yarusevych, "Vortex shedding from cylinders with two step discontinuities in diameter," J. Fluid Mech. **902**, A29 (2020).

[23] Y. Yan, C. Ji, and N. Srinil, "Three-dimensional flip-flopping flow around a pair of dual-stepped circular cylinders in a side-by-side arrangement," Phys. Fluids **32**, 123608 (2020).

[24] C. Morton, S. Yarusevych, and I. Carvajal-Mariscal, "Study of flow over a step cylinder," Appl. Mech. Mater. **15**, 9–14 (2009).

[25] J. McClure, C. Morton, and S. Yarusevych, "Flow development and structural loading on dual step cylinders in laminar shedding regime," Phys. Fluids **27**, 063602 (2015).

[26] C. Ji, Y. Cui, D. Xu, X. Yang, and N. Srinil, "Vortex-induced vibrations of dual-step cylinders with different diameter ratios in laminar flows," Phys. Fluids **31**, 073602 (2019).

[27] C. Ji, X. Yang, Y. Yu, Y. Cui, and N. Srinil, "Numerical simulations of flows around a dual step cylinder with different diameter ratios at low Reynolds numbers," Eur. J. Mech.-B/Fluids **79**, 332–344 (2020).

[28] D. Sumner and J. Heseltine, "Tip vortex structure for a circular cylinder with a free end," J. Wind. Eng. Ind. Aerodyn. **96**, 1185–1196 (2008).

[29] D. Sumner, J. Heseltine, and O. Dansereau, "Wake structure of a finite circular cylinder of small aspect ratio," Exp. Fluids **37**, 720–730 (2004).

[30] D. Zhang, L. Cheng, H. An, and M. Zhao, "Direct numerical simulation of flow around a surface-mounted finite square cylinder at low Reynolds numbers," Phys. Fluids **29**, 045101 (2017).

[31] C. Part and S. Lee, "Flow structure around a finite circular cylinder embedded in various atmospheric boundary layers," Fluid Dyn. Res. **30**, 197–215 (2002).

[32] S. Krajnovic, "Flow around a tall finite cylinder explored by large eddy simulation," J. Fluid Mech. **676**, 294–317 (2011).

[33] R. Hain, C. Kähler, and D. Michaelis, "Tomographic and time resolved PIV measurements on a finite cylinder mounted on a flat plate," Exp. Fluids **45**, 715–724 (2008).

[34] D. Sumner, "Flow above the free end of a surface-mounted finite-height circular cylinder: A review," J. Fluids Struct. **43**, 41–63 (2013).

[35] J. Bourgeois, P. Sattari, and R. Martinuzzi, "Alternating half-loop shedding in the turbulent wake of a finite surface-mounted square cylinder with a thin boundary layer," Phys. Fluids **23**, 095101 (2011).

[36] M. Manhart and R. Friedrich, "DNS of a turbulent boundary layer with separation," Int. J. Heat Fluid Flow **23**, 572–581 (2002).

[37] M. Manhart, "A zonal grid algorithm for DNS of turbulent boundary layers," Comput. Fluids **33**, 435–461 (2004).

[38] J. H. Williamson, "Low-storage Runge-Kutta schemes," J. Comput. Phys. **35**, 48–56 (1980).

[39] H. L. Stone, "Iterative solution of implicit approximations of multidimensional partial differential equations," SIAM J. Numer. Anal. **5**, 530–558 (1968).

[40] N. Peller, A. L. Duc, F. Tremblay, and M. Manhart, "High-order stable interpolations for immersed boundary methods," Int. J. Numer. Meth. Fl. **52**, 1175–1193 (2006).

[41] J. P. Gallardo, H. I. Andersson, and B. Pettersen, "Turbulent wake behind a curved circular cylinder," J. Fluid Mech. **742**, 192–229 (2014).

[42] F. Jiang, B. Pettersen, and H. I. Andersson, "Turbulent wake behind a concave curved cylinder," J. Fluid Mech. **878**, 663–699 (2019).

[43] J. C. R. Hunt, A. Wray, and P. Moin, "Eddies, stream, and convergence zones in turbulent flows," Center for Turbulent Research Report CTR-S88, 193–208, 1988.

[44] D. Sujudi and R. Haimes, "Identification of swirling flow in 3-d vector fields," in *12th Computational Fluid Dynamics Conference, San Diego, CA, June 19–22* (AIAA, Reston, VA, 1995), p. 1715.

[45] J. Ishii and S. Honami, "A three-dimensional turbulent detached flow with a horseshoe vortex," J. Eng. Gas Turbines Power **108**, 125–130 (1986).

[46] R. L. Simpson, "Junction flows," Annu. Rev. Fluid Mech. **33**, 415–443 (2001).

[47]T. J. Praisner and C. R. Smith, "The dynamics of the horseshoe vortex and associated endwall heat transfer-part ii: Time-mean results," J. Turbomach. **128**, 755–762 (2006).
[48]A. Sau, R. Hwang, T. Sheu, and W. Yang, "Interaction of trailing vortices in the wake of a wall-mounted rectangular cylinder," Phys. Rev. E **68**, 056303 (2003).
[49]G. Palau-Salvador, T. Stoesser, J. Fröhlich, M. Kappler, and W. Rodi, "Large eddy simulations and experiments of flow around finite-height cylinders," Flow Turbul. Combust. **84**, 239 (2010).
[50]V. Dousset and A. Pothérat, "Formation mechanism of hairpin vortices in the wake of a truncated square cylinder in a duct," J. Fluid Mech. **653**, 519–536 (2010).
[51]W. Gretta and C. Smith, "The flow structure and statistics of a passive mixing tab," J. Fluids Eng. **115**, 255–263 (1993).
[52]R. Elavarasan and H. Meng, "Flow visualization study of role of coherent structures in a tab wake," Fluid Dyn. Res. **27**, 183 (2000).
[53]T. Wei and C. Smith, "Secondary vortices in the wake of circular cylinders," J. Fluid Mech. **169**, 513–533 (1986).
[54]J. McClure, C. Pavan, and S. Yarusevych, "Secondary vortex dynamics in the cylinder wake during laminar-to-turbulent transition," Phys. Rev. Fluids **4**, 124702 (2019).
[55]S. Robinson, "Coherent motions in the turbulent boundary layer," Annu. Rev. Fluid Mech. **23**, 601–639 (1991).
[56]C. Morton and S. Yarusevych, "Three-dimensional flow and surface visualization using hydrogen bubble technique," J. Vis. **18**, 47–58 (2015).